



# Numerical modeling of a proton exchange membrane fuel cell with tree-like flow field channels based on an entropy generation analysis



Cesar E. Damian-Ascencio <sup>a</sup>, Adriana Saldaña-Robles <sup>b</sup>, Abel Hernandez-Guerrero <sup>a</sup>, Sergio Cano-Andrade <sup>a,\*</sup>

<sup>a</sup> Department of Mechanical Engineering, Universidad de Guanajuato, Salamanca, Gto. 36885, Mexico

<sup>b</sup> Department of Agricultural Engineering, Universidad de Guanajuato, Irapuato, Gto. 36500, Mexico

## ARTICLE INFO

### Article history:

Received 17 September 2016

Received in revised form

27 April 2017

Accepted 22 May 2017

Available online 26 May 2017

### Keywords:

PEM fuel cell

Flow distributors

Tree-like pattern

Entropy generation

## ABSTRACT

This paper presents a three-dimensional numerical modeling of a PEM fuel cell with tree-like flow field channels. Four different tree-like configurations are considered for the study based on a statistical analysis of the veins of the leaves of different trees. The number of bifurcations of the vein and their inclination are considered as parameters for the characterization. Four different configurations are the most recurrent, corresponding to one level of bifurcation at 37° and 74° and two levels of bifurcation at 37° and 74°. The model considers a complete solution of the mass, momentum, energy, and electro-chemical equations. An entropy generation analysis is developed as a post processing once the solution of the models is obtained. Because new geometries for the channel configuration in the bipolar plates are introduced, special attention is considered for the entropy generation due to mass flow. Results indicate that the configuration with two levels of bifurcation at 37° is efficient at removing water from the cathode channels, resulting in a good current density production. In addition, a better performance of the PEM fuel cell (higher current density production and lower entropy production) is obtained by increasing the number of bifurcations.

© 2017 Elsevier Ltd. All rights reserved.

## 1. Introduction

A proton exchange membrane (PEM) fuel cell is an electro-chemical device that directly converts the chemical energy of hydrogen into electricity without the need of a combustion process [1,2]. PEM fuel cells are a promising substitute for fossil-fueled technologies because of their relatively high efficiency (40–60%), fast start-up, silent performance, near-zero emissions to the environment (residues are only liquid water and heat), and they are not limited by the Carnot efficiency [1,2]. PEM fuel cells are also a good alternative when coupled with other technologies in form of microgrids [3–6].

The main drawbacks of a PEM fuel cell to date are the high investment costs and short periods of durability associated with the materials (especially for the platinum in the catalyst layers that is expensive and is highly affected by CO<sub>2</sub> poisoning), and also the non-homogeneous current density production due to an

inadequate distribution of the reactants in the fuel cell [1,2,7]. With respect to the latter, the shape of the channel cross sectional area, the channel dimensions, and the gas flow channel configuration have to be properly designed. The motivation of the present work is on the design of the gas flow channel configuration, where much effort has been devoted during the past years [8–10].

For the gas flow channels, four configurations are considered as conventional, i.e., straight, parallel, serpentine, and interdigitated. The straight channel configuration [11,12] provides a good production and distribution of current density, but its main limitation is the geometry itself because a very long channel is needed to produce an acceptable amount of energy. However, the straight channel configuration is the base for most of the subsequent geometries proposed. The parallel channels configuration [13–15] provides a high current density production, but presents zones of water accumulation and, as a consequence, a non-uniform current density production. The serpentine configuration [13,15–18] provides a high current density production and a good removal of the water generated at the cathode, but its main drawback is the high pressure drop for the gas flow due to the length of the channel and the many sharp turns along the path. The interdigitated

\* Corresponding author.

E-mail address: [sergio.cano@ugto.mx](mailto:sergio.cano@ugto.mx) (S. Cano-Andrade).

configuration [8,19–23] is a modification of the parallel channels configuration that forces the gases to pass through the porous media, improving the water removal and having a better use of the reactants, but its main limitation is the high pressure drop for the gas flow which limits the overall performance of the fuel cell.

New gas flow channel configurations are proposed as an alternative to the conventional geometries. A radial configuration [24] shows a low pressure drop for the gas flow and areas of high current density production, but also areas where water is accumulated, showing a negligible current density production in these areas. A spiral configuration [13,25] allows the PEM fuel cell to have an uniform current density production on the active area and a low pressure drop for the gas flow, but still the overall fuel cell performance is limited. A parallel channel configuration in which the injection of the gases to the channels is modified in order to have a more uniform and homogeneous flow distribution in all the channels [26], and Pin-type configurations [13,27], provide an uniform current density production and a low pressure drop for the gas flow, but the overall fuel cell performance is still limited. A maze flow configuration [15] shows a rapid voltage decay at high values of current density, thus, presenting a very poor overall fuel cell performance. Other alternatives are to combine gas flow geometries, for instance, serpentine (anode) and interdigitated channels (cathode) [28], which show a good fuel cell performance in terms of water removal. Recently, porous media instead of channels are also proposed as gas flow distributors [29–31], showing a good mass distribution of both, hydrogen and oxygen, as well as a good overall fuel cell performance.

Biomimetic configurations [32] are also proposed as an alternative to the conventional geometries. These configurations are inspired on the observation of nature, under the premise that systems that reflect the natural configuration of biological systems are more efficient [33]. Biomimetic geometries are obtained using a deterministic principle for the generation (optimization) of geometric form in natural systems, limited to global and local constraints in order to improve the performance of the system under analysis [33]. Along this line, a tree-like pattern which results from a multiparametric optimization [34,35] shows a reduction of the pressure drop and a maximization of the net power produced. Fractal geometries based on respiratory systems [36,37] provide a low pressure drop for the flow of gases, but large areas of the cell are not used well, obtaining a non-uniform current density production. Other fractal geometries [38] produce a flooding of the channels due to the poor water management of the geometry. A configuration based on the geometry of the veins of leaves [39] provides a good performance of the fuel cell, but for the particular geometry proposed, the water management is not efficient because areas of water stagnation are present.

Although all these different non-conventional configurations for the gas flow channels, including nature-based and non-nature-based configurations, provide improvements for the PEM fuel cell performance, they still are not able to provide a better fuel cell performance than the conventional serpentine configuration. Also, only numerical studies are presented for most of these non-conventional geometries, leaving experimental studies as an open area of research.

In this paper, an analysis of the performance of a PEM fuel cell using four different tree-like configurations for the gas flow distributors is presented. The channel configurations mimic the distribution of the veins of a leaf, and consist of configuration models with one and two bifurcations and with two different angles for the inclination of the veins with respect to the main channel.

The paper is organized as follows: section 2 presents a description of the PEM fuel cell system under analysis; section 3 outlines the mathematical model used for the analysis; section 4

presents the numerical results of the PEM fuel cell performance with the four different configurations, including an entropy generation analysis; and section 5 concludes the paper.

## 2. System description

In order to define the tree-like configurations for the flow field channels, 30 of the most common trees in the Bajío region of México are randomly chosen, and 20 leaves from each tree are photographed. Measurements of the number of bifurcations and the bifurcation angles of the veins of a leaf are taken for all the images from the collection of pictures obtained for the analysis. The data is analyzed to define the most recurrent number of bifurcations and their inclination angles.

With respect to the number of bifurcations on the veins of leaves, two different configurations are found as the most statistically repetitive, i.e., a configuration with one level of bifurcation (one main channel and one flow branch), and a configuration with two levels of bifurcation (one main channel and two flow branches). A configuration with three levels of bifurcation is not studied because it causes the channels to cross with each other, thus, causing turbulence and instabilities in the gas flows. These instabilities cause that the PEM fuel cell reduce its current density production because the gases are not uniformly distributed on the active area. With respect to the bifurcation angles, the leaves collected are categorized in two sets. For the first set of leaves, the mean value of the bifurcation angle is  $37^\circ$  and the standard deviation is  $0.823^\circ$ , with a confidence interval of 95%. For the second set of leaves, the mean value of the bifurcation angle is  $74^\circ$  and the standard deviation is  $0.947^\circ$ , with a confidence interval of 95%.

The combination of the number of bifurcations and the different angles results in four different configurations for the flow channels, that is, one level of bifurcation at  $37^\circ$  and at  $74^\circ$  (Fig. 1a) and two levels of bifurcation at  $37^\circ$  and at  $74^\circ$  (Fig. 1b).

The PEM fuel cell system consists of current collectors, flow channels, diffusion layers, and catalyst layers for each side of the cell (anode and cathode), and a membrane between the catalyst layers. The catalyst layers are 0.03-mm thick, the diffusion layers are 0.5-mm thick, and the membrane is 0.05-mm thick. The total active area for the PEM fuel cell is  $9\text{-cm}^2$  for all configurations. The flow channel configuration at the anode is chosen to be the same than that at the cathode. The cross sectional area of the flow channels is square ( $1 \times 1\text{ mm}$  for the main vein), and decreases according to Murray's Law [40,41] by a factor of  $2^{-1/3}$  from one branch to the other. The branches are at the same level with the main vein. The design of the bifurcations are in line with the

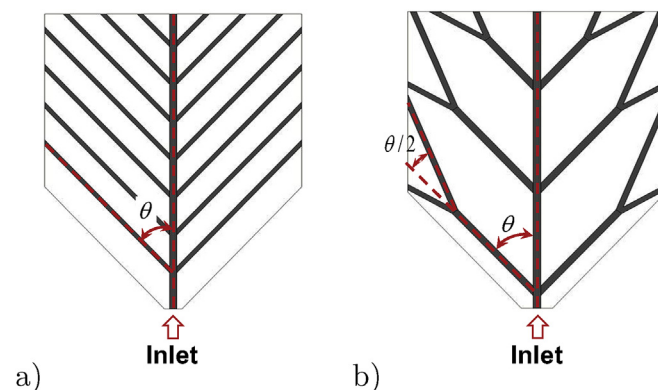


Fig. 1. Channel flow field pattern with: a) one level of bifurcation at  $\theta = 37^\circ$  (or  $74^\circ$ ) and b) two levels of bifurcations at  $\theta = 37^\circ$  (or  $74^\circ$ ).

methodology presented in Ref. [42] for one and two levels of bifurcation.

### 3. Mathematical model

#### 3.1. Model assumptions

The numerical modeling of the four different configurations for the PEM fuel cell system is developed under 1) steady state conditions; 2) single-phase with negligible gravity effects (although a real operation of a PEM fuel cell is a two-phase phenomenon with liquid and vapor, it has been proven that a single phase with vapor only is a good assumption for the analysis [43,44]); 3) laminar flow conditions in all domains of the cell; 4) transport of species (protons and other molecules) across the membrane is taken into account by means of source terms in the transport equations; 5) four species are considered for the reactions, i.e., H<sub>2</sub>, O<sub>2</sub>, N<sub>2</sub>, and H<sub>2</sub>O-vapor; 6) ideal gas behavior is used to determine the density of the gas mixture at every control volume in the domain; 7) gas mixture viscosity is calculated using ideal-gas-mixing law; and 8) non-isothermal conditions exist in the cell domain.

#### 3.2. Governing equations for the CFD model

The governing equations and source terms of the CFD model that describe the physical phenomena taking place in a fuel cell are given in Table 1. A schematic representation of the fuel cell domain and the location of the source terms,  $r_k$  (where  $1 \leq k \leq 5$ ), is given in Fig. 2.

The density of the mixture is defined as:

$$\rho = \left( \sum_{\xi} \frac{Y_{\xi}}{\rho_{\xi}} \right)^{-1} \quad (14)$$

and the viscosity of the mixture:

$$\mu = \sum_{\xi} Y_{\xi} \mu_{\xi} \quad (15)$$

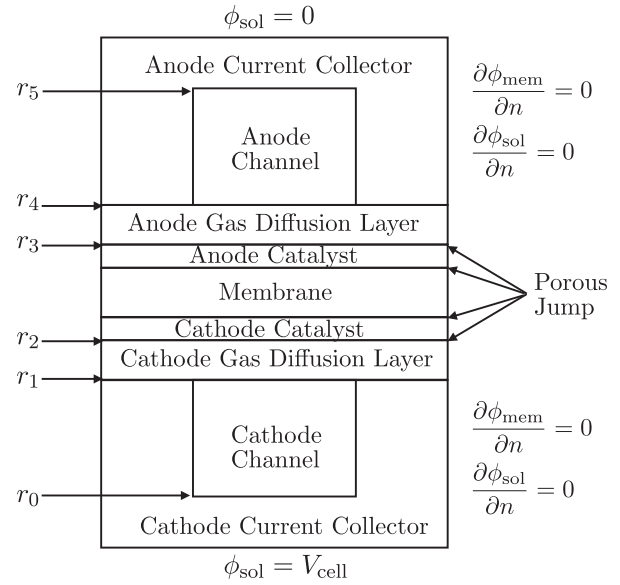


Fig. 2. Representation of the computational domain for the model, locations where the source terms are applied, and boundary conditions.

In Equation (2), the permeability,  $\beta$ , is considered to be homogeneous. The diffusion mass flux of specie  $\xi$  in Equation (3) is defined as:

$$\vec{J}_{\xi} = -\rho D_{\xi} \vec{\nabla} Y_{\xi} \quad (16)$$

and the diffusion coefficient in the porous media is given as [45]:

$$D_{\xi} = \epsilon^{1.5} D_{\xi}^0 \left( \frac{P_0}{P} \right) \left( \frac{T}{T_0} \right)^{3/2} \quad (17)$$

where the reference pressure and reference temperature are 1 atm and 300 K, respectively.

The exchange current density at the anode side in Equations (4),

Table 1  
Governing equations of the model.

Equation	Mathematical Expression	Source Terms
Momentum	$(\vec{u} \cdot \vec{\nabla}) \rho \vec{u} = -\vec{\nabla} P + \vec{\nabla} (\mu \vec{\nabla} \cdot \vec{u}) + \vec{S}_{Mo} \quad (1)$	$\vec{S}_{Mo} = -\frac{\mu}{\beta} \vec{u} \text{ at } r_1 \leq r \leq r_4 \quad (2)$
Transport of species	$(\vec{u} \cdot \vec{\nabla}) \rho Y_{\xi} = \vec{\nabla} \cdot \vec{J}_{\xi} + S_{\xi} \quad (3)$	$S_{H_2} = -\frac{M_{H_2}}{2F} R_a \text{ at } r_3 \quad (4)$ $S_{O_2} = -\frac{M_{O_2}}{4F} R_c \text{ at } r_2 \quad (5)$ $S_{H_2O,a} = -\frac{M_{H_2O}}{F} R_a \text{ at } r_3 \quad (6)$ $S_{H_2O,c} = \frac{M_{H_2O}}{2F} R_c \text{ at } r_2 \quad (7)$
Conservation of mass	$\vec{\nabla} \cdot (\rho \vec{u}) = S_m \quad (8)$	$S_m = S_{H_2} + S_{H_2O,a} \text{ at } r_3 \quad (9a)$ $S_m = S_{O_2} + S_{H_2O,c} \text{ at } r_2 \quad (9b)$
Solid phase potential	$\vec{\nabla} \cdot (\sigma_{sol} \vec{\nabla} \phi_{sol}) + S_{sol} = 0 \quad (10)$	$S_{sol} = -R_a \text{ at } r_3 \quad (11a)$ $S_{sol} = R_c \text{ at } r_2 \quad (11b)$
Membrane phase potential	$\vec{\nabla} \cdot (\sigma_{mem} \vec{\nabla} \phi_{mem}) + S_{mem} = 0 \quad (12)$	$S_{mem} = R_a \text{ at } r_3 \quad (13a)$ $S_{mem} = -R_c \text{ at } r_2 \quad (13b)$

(6), (11a), and (13a) is obtained from the Butler-Volmer equation, and is defined as:

$$R_a = j_a^{\text{ref}} \left( \frac{[H_2]}{[H_2]_{\text{ref}}} \right)^{\gamma_a} \left[ \exp\left(\frac{\alpha_a F \eta_a}{RT}\right) - \exp\left(-\frac{\alpha_c F \eta_c}{RT}\right) \right] \quad (18)$$

and the exchange current density at the cathode side in Equations (5), (7), (11b), (13b) is also obtained from the Butler-Volmer equation, and is defined as:

$$R_c = j_c^{\text{ref}} \left( \frac{[O_2]}{[O_2]_{\text{ref}}} \right)^{\gamma_c} \left[ -\exp\left(\frac{\alpha_a F \eta_c}{RT}\right) + \exp\left(-\frac{\alpha_c F \eta_c}{RT}\right) \right] \quad (19)$$

where the water transfer coefficients for the anode and cathode sides are:

$$\alpha_a = n_d - \frac{F}{R_a} D_{H_2O} \frac{C_{H_2O,c} - C_{H_2O,a}}{t_m} \quad (20a)$$

$$\alpha_c = n_d - \frac{F}{R_c} D_{H_2O} \frac{C_{H_2O,c} - C_{H_2O,a}}{t_m} \quad (20b)$$

the water diffusion coefficient in the membrane is defined as [46]:

$$D_{H_2O} = 5.5 \times 10^{-11} n_d \exp\left[2416\left(\frac{1}{303} - \frac{1}{T}\right)\right] \quad (21)$$

the electroosmotic drag coefficient is defined as:

$$n_d = \frac{2.5}{22} \lambda \quad (22)$$

the water concentration at the anode and cathode sides is defined as:

$$C_{H_2O,(a,c)} = \frac{\rho_m \cdot \text{dry}}{M_m \cdot \text{dry}} \lambda \quad (23)$$

the water content in the membrane is given as [47]:

$$\lambda = 0.043 + 17.18 a_a - 39.85 a_a^2 + 36 a_a^3 \quad a_a \leq 1 \quad (24a)$$

$$\lambda = 14 + 1.4(a_a - 1) \quad a_a > 1 \quad (24b)$$

the water activity is given as:

$$a_a = \frac{X_{H_2O} P}{P_{\text{sat}}} \quad (25)$$

the saturation pressure of water vapor is defined as [47]:

$$\log_{10} P_{\text{sat}} = -2.1794 + 0.02953(T - 273.15) - 9.1837 \times 10^{-5}(T - 273.15)^2 + 1.4454 \times 10^{-7}(T - 273.15)^3 \quad (26)$$

the surface overpotentials at the anode and cathode sides are defined as:

$$\eta_a = \phi_{\text{sol}} - \phi_{\text{mem}} \quad (27a)$$

$$\eta_c = \phi_{\text{sol}} - \phi_{\text{mem}} - V_{\text{oc}} \quad (27b)$$

and the reference open-circuit voltage of the fuel cell at low temperature operations is given as [48]:

$$V_{\text{oc}} = 0.0025T + 0.2329 \quad (28)$$

Finally, the membrane electric conductivity in Equation (12) is defined as [47]:

$$\sigma_{\text{mem}} = \epsilon(0.5139\lambda - 0.326)\exp\left[1268\left(\frac{1}{303} - \frac{1}{T}\right)\right] \quad (29)$$

### 3.3. Entropy generation model

The entropy generation analysis is implemented as a post-processing once the CFD simulations for the fuel cell system with the four different gas flow configurations are obtained. The entropy generation is defined as [49]:

$$S_{\text{gen}} = \vec{q} \cdot \vec{\nabla} \left( \frac{1}{T} \right) - \sum_{\xi} \vec{J}_{\xi} \cdot \vec{\nabla} \left( \frac{\mu_{\xi}}{T} \right) - \frac{1}{T} P^{\nu} \cdot \vec{\nabla} \nu - P_0^{\nu} : \vec{\nabla} \nu \quad (30)$$

where the first term in the right-hand side accounts for the entropy generation due to heat transfer, the second term accounts for the entropy generation due to mass flow, and the third and fourth terms account for the entropy generation due to fluid friction. Thus, Equation (30) can be expressed as:

$$S_{\text{gen}} = S_{\text{gen}}^{\text{HT}} + S_{\text{gen}}^{\text{MF}} + S_{\text{gen}}^{\text{FF}} \quad (31)$$

A common parameter used to represent the irreversibilities in a system is the Bejan number [50], defined as:

$$Be = \frac{S_{\text{gen}}^{\text{HT}}}{S_{\text{gen}}} \quad (32)$$

where for this particular case  $S_{\text{gen}} = S_{\text{gen}}^{\text{HT}} + S_{\text{gen}}^{\text{FF}}$ . This parameter indicates that the irreversibilities due to heat transfer are dominant when  $Be > 1/2$  [33].

Since the purpose of the present work is to analyze the effect of new geometries for the gas flow channels in a PEM fuel cell, the parameter [51]:

$$\Pi = \frac{S_{\text{gen}}^{\text{MF}}}{S_{\text{gen}}} \quad (33)$$

is used as an indicator, where now  $S_{\text{gen}}$  is defined by Equation (31). The  $\Pi$  parameter suggests that the irreversibilities due to mass diffusion become dominant when  $\Pi > 1/3$ .

### 3.4. Boundary conditions

The external boundaries of the PEM fuel cell computational domain are considered as walls (see Fig. 2). The protonic current flow is constrained to be zero at these external boundaries, i.e.,  $\partial \phi_{\text{mem}} / \partial n = 0$ . The solid phase potential is also constrained to be zero at all external boundaries, i.e.,  $\partial \phi_{\text{sol}} / \partial n = 0$ , except at the upper surface of the cathode current collector (where  $\phi_{\text{sol}} = 0$ ) and at the upper surface of the anode current collector (where  $\phi_{\text{sol}} = V_{\text{cell}}$ , considering  $V_{\text{cell}} = 0.53$  V [16]), with the purpose to model the flux of electrons through an external circuit. To the inlet of the channels (anode and cathode) is given a boundary condition of fixed velocity perpendicular to the cross sectional area of the channels. To the outlet of the channels is given a boundary condition of zero pressure gauge, in order to emulate a flow discharge to the atmosphere. The layers of the porous media are considered as porous jumps [24,25].

**Table 2**  
Flow inlet conditions used for the present model.

	Flow Conditions	Very Low Humidity	Low Humidity	High Humidity	Very High Humidity
Anode	Velocity of gas mixture ( $\text{m s}^{-1}$ )	1.735	1.83	2.21	2.56
	Mass Fraction $\text{H}_2$	0.7288	0.637	0.4076	0.2964
	Mass Fraction $\text{H}_2\text{O}$	0.2712	0.363	0.5924	0.7036
Cathode	Velocity of gas mixture ( $\text{m s}^{-1}$ )	7.33	7.91	9.05	12.9
	Mass Fraction $\text{O}_2$	0.3021	0.2881	0.2638	0.2086
	Mass Fraction $\text{H}_2\text{O}$	0.649	0.6179	0.5695	0.4385
	Mass Fraction $\text{N}_2$	0.0489	0.09404	0.1667	0.3529

### 3.5. Operating conditions

For the four PEM fuel cell configurations presented in this paper (i.e., one and two bifurcations with bifurcation angles of  $37^\circ$  and  $74^\circ$ ), four different flow inlet conditions are used according with the values reported by Shimpalee et al. [16]. These inlet conditions correspond to cases of very high humidity, high humidity, low humidity, and very low humidity. The numerical values for the four humidity cases are reported in Table 2, and the electrochemical properties for the model are given in Table 3. It is considered that the fuel cell operates at a pressure of 2 atm and a temperature of 343 K.

### 3.6. Numerical procedure

The governing equations of the PEM fuel cell model in their discretized form are solved numerically using a commercial code based on the finite volume method. An add-on PEM fuel cell routine is used with the commercial software to include the electrochemical parameters for the source terms. The SIMPLE algorithm is used for the solution of the equations. This algorithm uses a relationship between velocity and pressure corrections to ensure mass conservation and to obtain the correct pressure at each iteration of the cycle. For each iteration, the momentum equation in the three directions is solved; then, a correction for the pressure is calculated keeping a correct mass balance; next, the transport of species equation is solved with the corrected data from the previous steps; finally, the solid phase and membrane phase potential equations are solved to complete the iteration of the cycle. The iterative cycle continues until convergence is reached. Once the CFD simulations of the system are obtained, the entropy generation analysis for each of the four different gas flow configurations is developed as a post-processing manner using a commercial code. Due to the symmetry

of the geometry, only half of the PEM fuel cell is simulated to reduce the computational burden associated with solving the complete system.

To ensure a grid independence solution, the mesh is varied increasing the number of elements until the change in the value of the current density between the new case and the previous one is less than 0.5%. For the four different PEM fuel cell configurations, the optimal mesh contains about 1,000,000 elements based on triangular prisms. Also, the mesh quality is checked in order to avoid having too many highly-skewed elements. All the elements in the mesh correspond to a quality less than 0.25 for the four different gas flow configurations, which corresponds to an excellent quality (a perfect quality of the mesh corresponds to a value of zero).

## 4. Results

### 4.1. Validation of the model

The CFD model used in this paper is validated with the data from Dutta et al. [11] for a straight channel PEM fuel cell. The straight channel PEM fuel cell model is constructed using the same dimensions, operating conditions, and material properties reported in Ref. [11]. The model consists of two flow channels, two diffusion layers, two catalyst layers, and a membrane between the two catalyst layers. Fig. 3 shows the results of the current density production along the length of the channel. Red triangles correspond to the values obtained with the CFD model of the present work, and black squares are the data from Dutta et al. [11]. The error of the CFD model used in this work is measured using the Sum of Squared Errors

$$\Gamma_{\text{SSE}} = \sum_i (y_i - \hat{y}_i)^2 \quad (34)$$

**Table 3**  
Values of the electrochemical parameters used for modeling the four different PEM fuel cell configurations.

Property	Symbol	Value
Current collector conductivity ( $\Omega^{-1} \text{ m}^{-1}$ ) [52]	$\sigma_{\text{sol}}$	$1.25 \times 10^5$
Gas diffusion layer conductivity ( $\Omega^{-1} \text{ m}^{-1}$ ) [52]	$\sigma_{\text{GDL}}$	53
Catalyst conductivity ( $\Omega^{-1} \text{ m}^{-1}$ ) [52]	$\sigma_{\text{cat}}$	53
Electrode porosity [24]	$\varepsilon$	0.7
Oxygen concentration dependence [53]	$\gamma_{\text{O}_2}$	1
Hydrogen concentration dependence [53]	$\gamma_{\text{H}_2}$	0.5
Anode transfer coefficient [53]	$\alpha_a$	2
Cathode transfer coefficient [53]	$\alpha_c$	2
Anode reference exchange current density ( $\text{A m}^{-3}$ ) [24]	$j_a^{\text{ref}}$	$2.0 \times 10^8$
Cathode reference exchange current density ( $\text{A m}^{-3}$ ) [24]	$j_c^{\text{ref}}$	$4.0 \times 10^6$
Permeability ( $\text{m}^2$ ) [24]	$\beta$	$2.0 \times 10^{-10}$
Hydrogen reference diffusivity ( $\text{m}^2 \text{ s}^{-1}$ ) [24]	$D_{\text{H}_2}^0$	$6.0 \times 10^{-5}$
Oxygen reference diffusivity ( $\text{m}^2 \text{ s}^{-1}$ ) [53]	$D_{\text{O}_2}^0$	$3.2 \times 10^{-5}$
Water reference diffusivity ( $\text{m}^2 \text{ s}^{-1}$ ) [24]	$D_{\text{H}_2\text{O}}^0$	$6.0 \times 10^{-5}$
Nitrogen reference diffusivity ( $\text{m}^2 \text{ s}^{-1}$ ) [24]	$D_{\text{N}_2}^0$	$8.0 \times 10^{-5}$



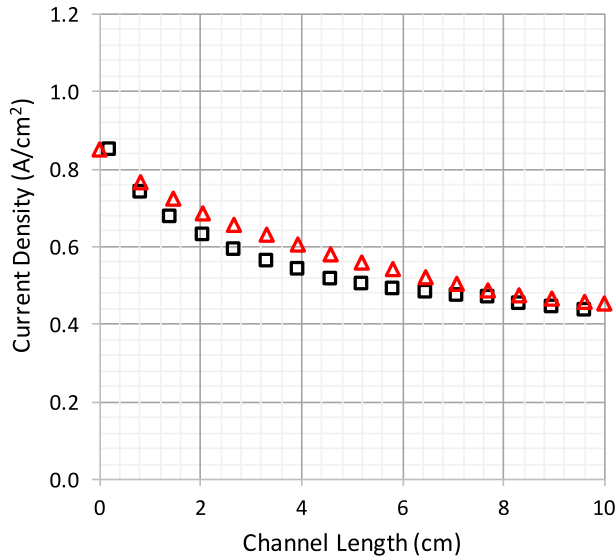


**Fig. 3.** Results for the validation of the present model (red triangles) with data from Dutta et al. [11] (black squares). (For interpretation of the references to colour in this figure legend, the reader is referred to the web version of this article.)

where  $i$  is the number of measurements,  $y_i$  is the value to be predicted, and  $\hat{y}_i$  is the predicted value of  $y_i$ . Results show that the current density production along the length of the channel is similar to that of Dutta et al. [11], with an error of  $\Gamma_{SSE} = 3.25\%$ , which indicates that the present model is able to predict well the performance of a PEM fuel cell system.

#### 4.2. Performance with one level of bifurcation

**Fig. 4** shows the current density contours for the PEM fuel cell model configuration with one level of bifurcation at  $37^\circ$ , and for each of the four flow inlet humidity conditions. The current density contours are obtained at the membrane. Results show that an increment in the flow inlet humidity causes an increase in the current density production of the PEM fuel cell. This is because the

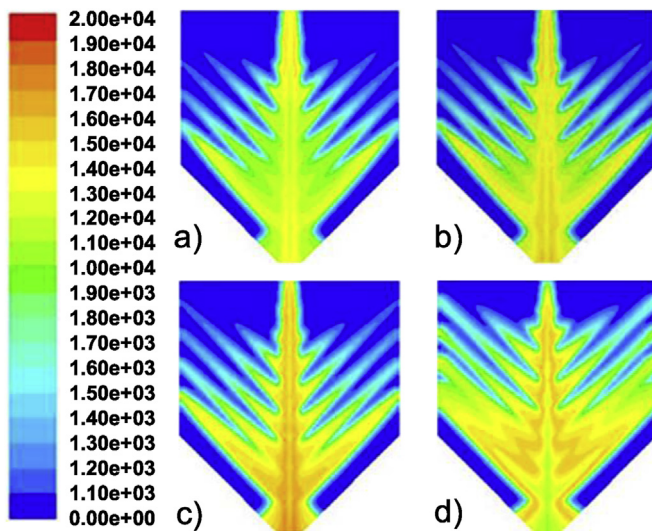


**Fig. 4.** Current density contours for the configuration with one level of bifurcation at  $37^\circ$ : a) very low humidity, b) low humidity, c) high humidity, and d) very high humidity conditions.

membrane's conductivity increases with the humidity of the gases, helping the kinetics of the reactions. The figure also shows that current density production is achieved more uniformly for the cases when the flow inlet humidity is increased.

**Fig. 5** shows the current density contours for the PEM fuel cell model configuration with one level of bifurcation at  $74^\circ$ , and for each of the four flow inlet humidity conditions. The current density contours are obtained at the membrane. Results show that current density production increases as the flow inlet humidity is increased. Interestingly, the current density production decreases to a very low value for the case of very low humidity. Compared with the configuration of one level of bifurcation at  $37^\circ$ , this configuration allows a better use of the reactant area because a more uniform distribution of the gases is achieved. Also, excluding the case of very low humidity, a higher current density production is achieved when compared with the configuration of one level of bifurcation at  $37^\circ$ .

#### 4.3. Performance with two levels of bifurcation

**Fig. 6** shows the current density contours for the PEM fuel cell model with two levels of bifurcation at  $37^\circ$ , and for the four flow inlet humidity conditions. The current density contours are obtained at the membrane. Results show that an increase in the flow inlet humidity condition causes an increase in the current density production. Comparing this configuration with that of one level of bifurcation at  $37^\circ$ , a higher current density production is observed. In addition, this configuration, as the one with one level of bifurcation at  $37^\circ$ , shows zones where current density production is negligible, having an inadequate use of the available area of reaction.

**Fig. 7** shows the current density contours for the PEM fuel cell model with two levels of bifurcation at  $74^\circ$ , for the four flow inlet humidity conditions. The current density contours are obtained at the membrane. Results show that the reaction area is used uniformly in the location of the bifurcations, as a consequence of a better redistribution of the gases. Similar to the configurations of one and two levels of bifurcation at  $37^\circ$ , this configuration shows areas where the current density production is very low, reducing the overall efficiency of the PEM fuel cell. For this configuration, higher values of current density production are obtained near the

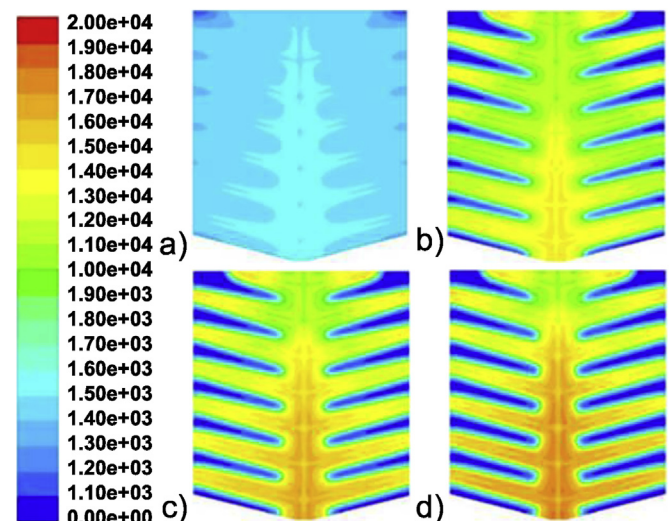


**Fig. 5.** Current density contours for the configuration with one level of bifurcation at  $74^\circ$ : a) very low humidity, b) low humidity, c) high humidity, and d) very high humidity conditions.

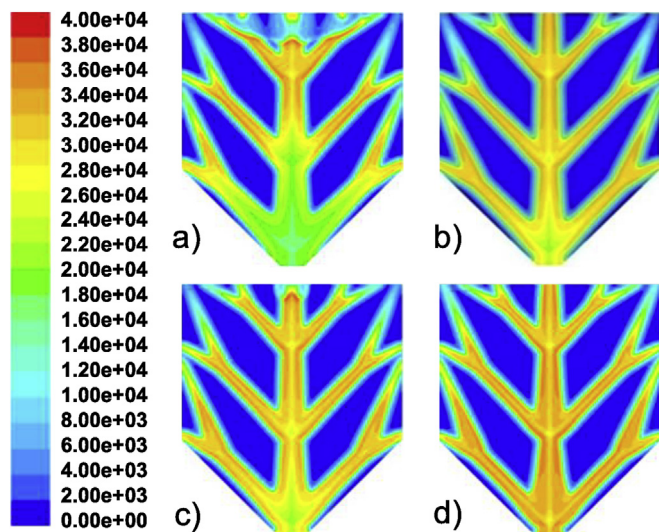


Fig. 6. Current density contours for the configuration with two levels of bifurcation at 37°: a) very low humidity, b) low humidity, c) high humidity, and d) very high humidity conditions.

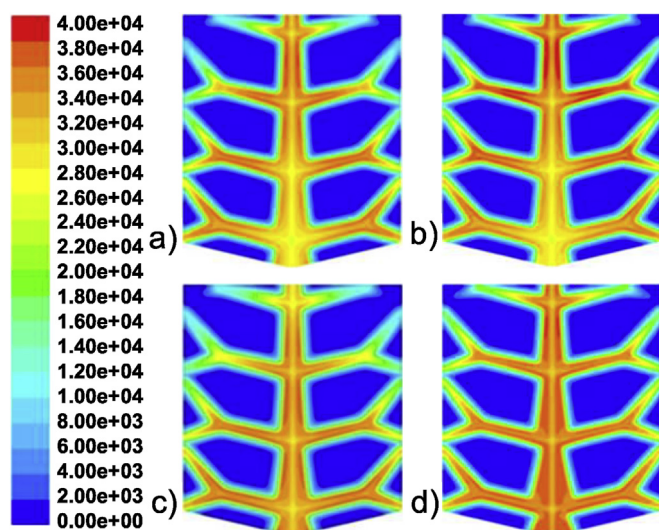


Fig. 7. Current density contours for the configuration with two levels of bifurcation at 74°: a) very low humidity, b) low humidity, c) high humidity, and d) very high humidity conditions.

location of the bifurcations. The figure also shows that this configuration produces a higher value of the current density than that of the configuration of one level of bifurcation at 74°.

#### 4.4. Comparison of the four different configurations

Table 4 shows a comparison of the average current density

**Table 4**  
Comparison of the average current density ( $A\ cm^{-2}$ ) for the different models presented.

	One Level at 37°	Two Levels at 37°	One Level at 74°	Two Levels at 74°
Very Low Humidity	0.79	1.16	0.86	1.06
Low Humidity	0.85	1.22	0.88	1.09
High Humidity	0.92	1.24	0.91	1.11
Very High Humidity	0.92	1.25	0.91	1.12

produced by the four different configurations at the four different operating (humidity) conditions. The best performance of the PEM fuel cell configurations is obtained at high and very high humidity conditions. For all four configurations, the performance with these two humidity conditions is almost the same. The configuration with two levels of bifurcation at 37° shows the best performance and the configuration with one level of bifurcation at 37° shows the poorest performance, both when compared to the other configurations at all four humidity conditions. The configurations with one level of bifurcation show a lower performance than the configurations with two levels of bifurcation.

Fig. 8 shows a comparison of the four different PEM fuel cell configurations at high humidity conditions because it is at this condition (like the case of very high humidity condition) where the best performance of the PEM fuel cell system is obtained. The figure shows that the larger current density production is obtained in areas right underneath the channels, and then gradually decrease for the zones far from the channels. It also shows that the current density production decreases faster for the configurations with one level of bifurcation than those with two levels of bifurcation. This indicates that the configurations with two levels of bifurcation have a better flow distribution for the reactants in the PEM fuel cell system. Also, larger angles of bifurcation present a limitation for the gases to flow, especially at the zones where the bifurcation is located, causing that most of the gas flow stay at the main channel.

Fig. 9 shows the water mass fraction contours in the channels at the cathode side where water is generated. Results suggest that the configurations with two levels of bifurcation contribute well for the removal of water from the channels. This adequate water removal is reflected in the high current density production of these configurations (see Figs. 6 and 7). On the contrary, the configurations with one level of bifurcation show accumulation of water at the end of

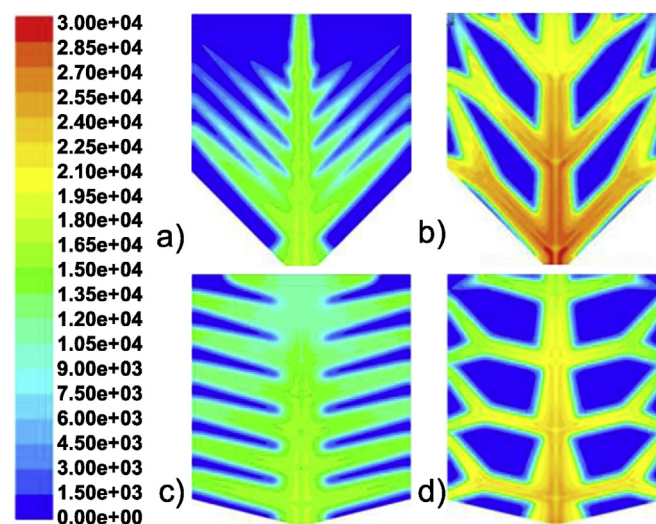
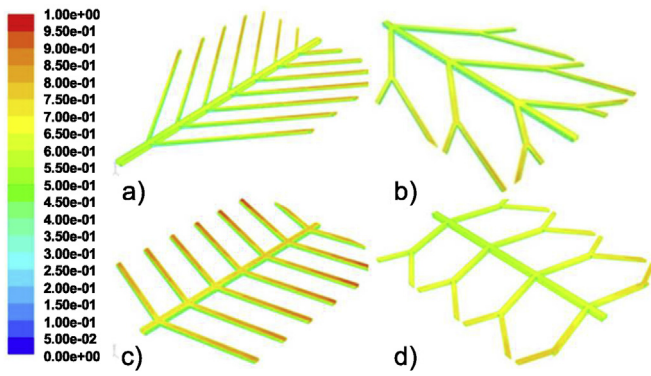


Fig. 8. Contours of current density at high humidity conditions for the configuration with: a) one level of bifurcation at 37°, b) two levels of bifurcation at 37°, c) one level of bifurcation at 74°, and d) two levels of bifurcation at 74°.





**Fig. 9.** Contours of  $\text{H}_2\text{O}$  mass fraction in the cathode channel at high humidity conditions for the configuration with: a) one level of bifurcation at  $37^\circ$ , b) two level of bifurcation at  $37^\circ$ , c) one level of bifurcation at  $74^\circ$ , and d) two level of bifurcation at  $74^\circ$ .

the channels. This accumulation of water inhibit the reactions, which is reflected in a low current density production of the PEM fuel cell system (see Figs. 4 and 5).

Fig. 10 shows the polarization and power curves for the four configurations at high humidity conditions. In agreement with the current density contours (see Fig. 8), the configurations with two levels of bifurcation have a better performance than the configurations with one level of bifurcation. Also, the configuration with two levels of bifurcation at  $37^\circ$  shows the best performance. The configuration with the highest concentration losses is that with one level of bifurcation at  $37^\circ$  because its polarization and power curves decay rapidly at high values of current density. The figure also shows that the net power density is improved as the number of bifurcations increases, having the best performance with the configuration of two levels of bifurcation at  $37^\circ$ .

#### 4.5. Comparison of results with data obtained from the literature

Fig. 11 shows a comparison of the polarization and power curves for the configuration with two levels of bifurcation at  $37^\circ$ , with data obtained from the literature. This configuration is selected for

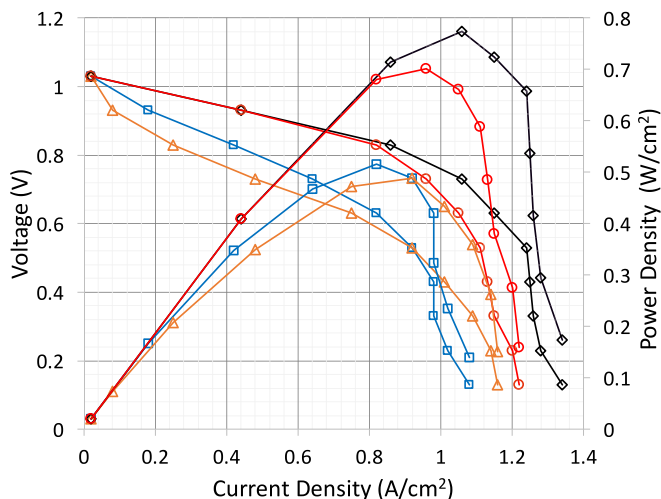


**Fig. 10.** Polarization and power curves at high humidity conditions for the configurations with one level of bifurcation at  $37^\circ$  (blue squares), one level of bifurcation at  $74^\circ$  (orange triangles), two levels of bifurcation at  $37^\circ$  (black diamonds), and two levels of bifurcation at  $74^\circ$  (red circles). (For interpretation of the references to colour in this figure legend, the reader is referred to the web version of this article.)

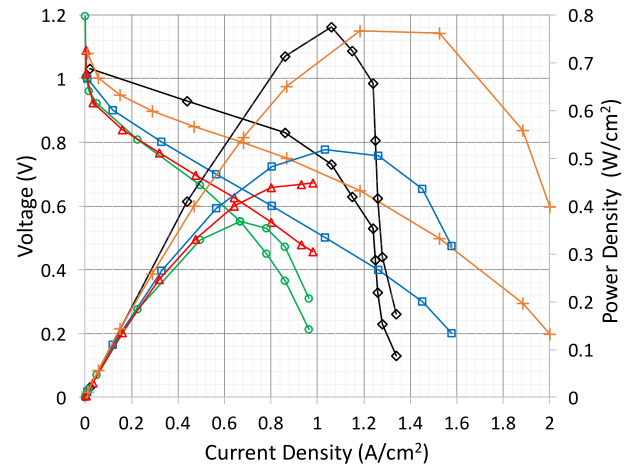


**Fig. 11.** Comparison of the polarization and power curves for the configuration with two levels of bifurcation at  $37^\circ$  (black diamonds), with data obtained from the literature: radial 4-channels configuration from Ref. [24] (orange +), spiral 4-channels configuration from Ref. [25] (blue squares), fractal 256-exits configuration from Ref. [36] (green circles), and parallel channels configuration from Ref. [53] (red triangles). (For interpretation of the references to colour in this figure legend, the reader is referred to the web version of this article.)

comparison because it is the configuration that shows the best performance from all four tree-like configurations proposed in this work.

Results show that the activation losses are almost the same for the five configurations, i.e., tree-like, radial, spiral, fractal, and parallel channels. However, the tree-like configuration with two levels of bifurcation at  $37^\circ$  proposed in this work shows the lowest amount of ohmic losses; while the fractal configuration shows the highest amount of ohmic losses. With respect to the concentration losses, the radial configuration shows the best performance, followed by the spiral configuration and the tree-like configuration. Since the purpose of proposing a new gas flow channel configuration is to reduce the concentration losses, results show that the tree-like configurations proposed in this work show a lower performance than other configurations found in the literature.

With respect to the power density production, the tree-like configuration proposed in this work shows the highest peak for the curve. However, its power curve decays rapidly at high values of current density because of concentration losses. The radial configuration shows the best overall performance from all five configurations, followed by the tree-like configuration. The fractal configuration shows the worst overall performance.

#### 4.6. Entropy generation analysis

Fig. 12 shows the entropy generation at high humidity conditions with an operational voltage of 0.73 V for the four different PEM fuel cell configurations analyzed in this paper. Fig. 12a shows the  $Be$  number (Equation (32)) which is an indicator of the entropy generation due to thermal effects. The smallest entropy generation due to thermal effects is obtained with the configuration of one level of bifurcation at  $37^\circ$ , while the configuration of one level of bifurcation at  $74^\circ$  presents the highest entropy generation due to thermal effects. The largest entropy generation is at the anode (channel, catalyst, and diffusion layer) because the exothermic reaction takes place at the anode side, thus, raising the temperature in the components. In general, for all four configurations, a small value of  $Be$  is obtained, which indicates that thermal effects are not dominant in a PEM fuel cell.

Fig. 12b shows the  $\Pi$  number (Equation (33)) which is an



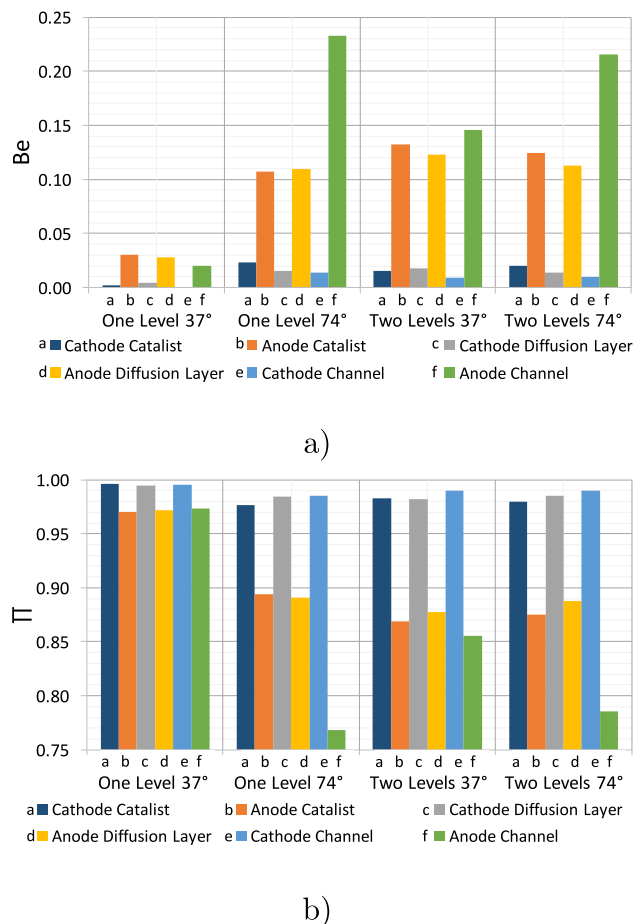


**Fig. 12.** Entropy generation at high humidity conditions for the four different PEM fuel cell configurations due to a) heat transfer and b) mass diffusion.

indicator of the entropy generation due to mass diffusion effects. Results show that the highest entropy generation due to mass diffusion is obtained with the configuration of one level of bifurcation at 37°, while the configuration of one level of bifurcation at 74° presents the lowest (see that the current density contour of Fig. 8c is more uniform than the current density contours of the other configurations in Fig. 8). Also, a higher value of  $\Pi$  is obtained at the anode side, mainly because the hydrogen is being consumed only at specific areas of the fuel cell, causing a nonuniform gas concentration for a major part of the reactive area. It can also be observed that the channels show the largest values of  $\Pi$  because they are responsible for the uniform distribution of the gases on the active area of the PEM fuel cell, suggesting that a good configuration increases the performance of the system.

The sum of the normalized values of all the different sources for entropy generation (thermal, mass flow, and fluid friction) is equal to one, and for the particular PEM fuel cell configurations presented in this work the entropy generation due to fluid friction is about the same magnitude as that due to thermal effects, suggesting that the mass flow effects are dominant in a PEM fuel cell system, especially those associated to the channel configuration. Thus, a better gas flow channel configuration is obtained for smaller values of  $\Pi$ .

## 5. Conclusions

A three-dimensional numerical model and an entropy generation analysis of a PEM fuel cell with tree-like flow field channels

was developed. The same channel configuration was used for the anode and cathode. The purpose of the analysis was to find a geometry that provides a good distribution of species for PEM fuel cells. The main findings of the study are as follows:

1. The angles and number of bifurcations most statistically repetitive for the branching of the nutrient channels in the tree leaves used for the analysis are one level of bifurcation at 37° and at 74°, and two levels of bifurcation at 37° and at 74°.
2. The gas flow channel configuration with two levels of bifurcation at 37° shows the best PEM fuel cell performance, and the gas flow channel configuration with one level of bifurcation at 37° shows the poorest PEM fuel cell performance.
3. Increasing the number of bifurcations provides a more uniform distribution of the reactant gases on the active area and, thus, a more uniform current density production. Increasing the angle of bifurcation reduces the overall performance of the fuel cell.
4. Entropy generation due to mass flow effects are dominant compared to thermal and fluid friction effects. A higher value of  $\Pi$  is obtained at the anode side (channel, catalyst, and diffusion layer). The channels show the largest values of  $\Pi$  because they are responsible for the uniform distribution of the gases on the active area of the PEM fuel cell.

The tree-like configurations proposed in this work show a lower overall performance than other configurations found in the literature. However, their performance is still comparable with these configurations. Thus, this comparable power production and the non-complex manufacturing make the tree-like geometries competitive for gas flow channel configurations in PEM fuel cells.

## Acknowledgments

S. Cano-Andrade, C.E. Damian-Ascencio, and Adriana Saldaña-Robles gratefully acknowledge to the SEP-PROMEP program (Mexico) under Grants No. UGTO-PTC-412, UGTO-PTC-524, and UGTO-PTC-565, respectively, and to the National Council of Science and Technology (CONACyT, Mexico) under the SNI program for financial support.

## Nomenclature

$H_2$	Hydrogen
$O_2$	Oxygen
$N_2$	Nitrogen
$H_2O$	Water
$r_k$	Location of source terms
$\vec{u}$	Velocity operator
$\vec{\nabla}$	Nabla operator
$\rho$	Density of the mixture
$\mu$	Viscosity of the mixture
$P$	Pressure
$P_0$	Reference pressure (1 atm)
$P_{sat}$	Saturation pressure
$T$	Temperature
$T_0$	Reference temperature (300 K)
$Y_\xi$	Mass fraction of specie $\xi$
$\rho_\xi$	Density of specie $\xi$
$\mu_\xi$	Viscosity of specie $\xi$
$\beta$	Permeability
$J_\xi$	Diffusion mass flux of specie $\xi$
$D_\xi$	Diffusion coefficient in the porous media for specie $\xi$
$D_\xi^0$	Diffusion coefficient at reference conditions for specie $\xi$
$\varepsilon$	Porosity of the media

$M_{H_2}$	Molecular weight of hydrogen
$M_{O_2}$	Molecular weight of oxygen
$M_{H_2O}$	Molecular weight of water
$F$	Faraday's constant (96,487 C mol <sup>-1</sup> )
$R_a$	Exchange current density at the anode side
$R_c$	Exchange current density at the cathode side
$j_a^{ref}$	Reference current density at the anode side
$j_c^{ref}$	Reference current density at the cathode side
$[H_2]$	Concentration of H <sub>2</sub>
$[H_2]_{ref}$	Reference concentration of H <sub>2</sub>
$[O_2]$	Concentration of O <sub>2</sub>
$[O_2]_{ref}$	Reference concentration of O <sub>2</sub>
$\gamma_a$	Concentration coefficient for the anode side
$\gamma_c$	Concentration coefficient for the cathode side
$\alpha_a$	Water transfer coefficient for the anode side
$\alpha_c$	Water transfer coefficient for the cathode side
$\eta_a$	Surface overpotential at the anode side
$\eta_c$	Surface overpotential at the cathode side
$R$	Universal gas constant
$n_d$	Electroosmotic drag coefficient
$t_m$	Membrane thickness
$\lambda$	Water content in the membrane
$C_{H_2O,a}$	Water concentration at the anode side
$C_{H_2O,c}$	Water concentration at the cathode side
$D_{H_2O}$	Water diffusion coefficient in the membrane
$\rho_{m,dry}$	Density of the dry membrane
$M_{m,dry}$	Weight of the dry membrane
$a_a$	Water activity
$X_{H_2O}$	Mole fraction of water
$\phi_{sol}$	Solid phase potential
$\phi_{mem}$	Membrane phase potential
$V_{oc}$	Reference open circuit voltage
$S$	Source term
$\sigma_{sol}$	Solid phase electric conductivity
$\sigma_{mem}$	Membrane electric conductivity
$I$	Average current density
$S_{gen}$	Entropy generation of the fuel cell
$S_{gen}^{HT}$	Entropy generation due to heat transfer
$S_{gen}^{MF}$	Entropy generation due to mass flow
$S_{gen}^{FF}$	Entropy generation due to fluid friction
$Be$	Bejan number
$\Pi$	Pi number
$\vec{q}$	Heat flux

### Subscripts / Superscripts

$k$	Number of source terms ( $1 \leq k \leq 5$ )
$\xi$	Type of specie (H <sub>2</sub> , N <sub>2</sub> , O <sub>2</sub> , H <sub>2</sub> O)
$\nu$	Stress tensor
$0$	Ambient conditions
$a$	Anode
$c$	Cathode
$sat$	Saturation
$ref$	Reference
$dry$	Dry
$sol$	Solid phase
$mem$	Membrane
$gen$	Generation
$Mo$	Momentum
$HT$	Heat transfer
$MF$	Mass flow
$FF$	Fluid friction

### References

- [1] Larminie J, Dicks A. Fuel cell systems explained. second ed. West Sussex, England: John Wiley & Sons Ltd.; 2003.
- [2] O'Hayre RP, Cha SW, Colella WG, Prinz FB. Fuel cells fundamentals. second ed. Hoboken, New Jersey: John Wiley & Sons Inc.; 2009.
- [3] Bruni G, Cordiner S, Mulone V. Domestic distributed power generation: effect of sizing and energy management strategy on the environmental efficiency of a photovoltaic-battery-fuel cell system. Energy 2014;77:133–43.
- [4] Bruni G, Cordiner S, Mulone V, Giordani A, Savino M, Tomarchio G, et al. Fuel cell based power system to supply power to telecom Station. Int J Hydrogen Energy 2014;39(36):21767–77.
- [5] Bruni G, Cordiner S, Mulone V, Rocco V, Spagnolo F. A study of energy management in domestic microgrids based on model predictive control strategies. Energy Convers Manag 2015;102:50–8.
- [6] Bruni G, Cordiner S, Mulone V, Sinisi V, Spagnolo F. Energy management in a domestic microgrid by means of model predictive controllers. Energy 2016;108:119–31.
- [7] Wilberforce T, Alaswad A, Palumbo A, Dassisti M, Olabi AG. Advances in stationary and portable fuel cell applications. Int J Hydrogen Energy 2016;41:16509–22.
- [8] Manso AP, Marzo FF, Barranco J, Garikano X, Garmendia Mujika M. Influence of geometric parameters of the flow fields on the performance of a PEM fuel cell. A review. Int J Hydrogen Energy 2012;37:15256–87.
- [9] Aiyejina A, Sastry MKS. PEMFC flow channel geometry optimization: a review. J Fuel Cell Sci Technol 2012;9(01011).
- [10] Arvay A, French J, Wang JC, Peng XH, Kannan AM. Nature inspired flow field designs for proton exchange membrane fuel cell. Int J Hydrogen Energy 2013;38:3717–26.
- [11] Dutta S, Shimpalee S, Van Zee JW. Three-dimensional numerical simulation of straight channel PEM fuel cells. J Appl Electrochem 2000;30(2):135–46.
- [12] Ferreira RB, Falcão DS, Oliveira VB, Pinto AMFR. Numerical simulations of two-phase flow in an anode gas channel of a proton exchange membrane fuel cell. Energy 2015;82:619–28.
- [13] Liu H, Li P, Juarez-Robles D, Wang K, Hernandez-Guerrero A. Experimental study and comparison of various designs of gas flow fields to PEM fuel cells and cell stack performance. Front Energy Res 2014;2(2):1–8.
- [14] Ferng YM, Su A. A three-dimensional full-cell CFD, model used to investigate the effects of different flow channel designs on PEMFC performance. Int J Hydrogen Energy 2007;32(17):4466–76.
- [15] Carton JG, Olabi AG. Design of experiment study of the parameters that affect performance of three flow plate configurations of a proton exchange membrane fuel cell. Energy 2010;35:2796–806.
- [16] Shimpalee S, Dutta S, Lee WK, Van Zee JW. Effect of humidity on PEM fuel cell performance: Part II - Numerical simulation. In: Proceedings of the ASME IMECE (heat transfer division)vol. 364; 1999. p. 367–74.
- [17] Maharudrayya S, Jayanti S, Deshpande AP. Pressure losses in laminar flow through serpentine channels in fuel cell stacks. J Power Sources 2004;138(1):1–13.
- [18] Cha D, Ahn JH, Kim HS, Kim Y. Effects of clamping force on the water transport and performance of a PEM (proton electrolyte membrane) fuel cell with relative humidity and current density. Energy 2015;93:1338–44.
- [19] Hu G, Fan J, Chen S, Liu Y. Three dimensional numerical analysis of proton exchange membrane fuel cells (PEMFCs) with conventional and interdigitated flow fields. J Power Sources 2004;136(1):1–9.
- [20] Wang JY, Wang HL. Flow field designs of bipolar plates in PEM fuel cells: theory and applications. Fuel cells 2012;12(6):989–1003.
- [21] Abdollahzadeh M, Pascoa JC, Ranjbar AA, Esmaili Q. Analysis of PEM (polymer electrolyte membrane) fuel cell cathode two-dimensional modeling. Energy 2014;68:478–94.
- [22] Djiali N. Computational modelling of polymer electrolyte membrane (PEM) fuel cells and opportunities. Energy 2007;23(4):269–80.
- [23] Ramiar A, Mahmoudi AH, Esmaili Q, Abdollahzadeh M. Influence of cathode flow pulsation on performance of proton exchange membrane fuel cell with interdigitated gas distributors. Energy 2016;94:206–17.
- [24] Cano-Andrade S, Hernandez-Guerrero A, von Spakovsky MR, Damian-Ascencio CE, Rubio-Arana JC. Current density and polarization curves for radial flow field patterns applied to PEMFCs (proton exchange membrane fuel cells). Energy 2010;35(2):920–7.
- [25] Juarez-Robles D, Hernandez-Guerrero A, Ramos-Alvarado B, Elizalde-Blancas F, Damian-Ascencio CE. Multiple concentric spirals for the flow field of a proton exchange membrane fuel cell. J Power Sources 2011;196:8019–30.
- [26] Ramos-Alvarado B, Hernandez-Guerrero A, Juarez-Robles D, Li P. Numerical investigation of the performance of symmetric flow distributors as flow channels for PEM fuel cells. Int J Hydrogen Energy 2012;37:436–48.
- [27] Lobato J, Canizares P, Rodrigo MA, Pinar FJ, Mena E, Ubeda D. Three-dimensional model of a 50 cm<sup>2</sup> high temperature PEM fuel cell. Study of the flow channel geometry influence. Int J Hydrogen Energy 2010;35:5510–20.
- [28] Chen S, Zhang X, Liu H. Effect of pressure difference between adjacent channels in an adjustable flow field in PEM fuel cells. Int J Hydrogen Energy 2017;42:4667–72.
- [29] Carton JG, Olabi AG. Three-dimensional proton exchange membrane fuel cell model: comparison of double channel and open pore cellular foam flow plates. Energy 2016:1–11.
- [30] Wilberforce T, Al Makky A, Baroutaji A, Sami R, Olabi AG. Optimisation of bipolar plate through computational fluid dynamic simulation and modelling using nickle open pore cellular foam material. In: International conference on renewable energies and power quality (ICREPQ'17), Malaga, Spain; 4–6 April

- 2017.
- [31] Wilberforce T, Al Makky A, Baroutaji A, Sambhi R, Olabi AG. Computational fluid dynamic simulation and modelling (CFX) of flow plate in PEM fuel cell using aluminum open cellular foam material. In: IEEE Texas power and energy conference (TPEC), College Station, TX, USA; 9–10 February 2017.
- [32] Chapman A, Mellor I. Development of biomimetic flow field plates for PEM fuel cells. In: Eighth grove fuel cell symposium; September 2003 [London, UK].
- [33] Bejan A. Shape and structure, from engineering to Nature. Cambridge: Cambridge University Press; 2000.
- [34] Senn SM, Poulidakos D. Tree network channels as fluid distributors constructing double-staircase polymer electrolyte fuel cells. *J Appl Phys* 2004;96(1):842–52.
- [35] Senn SM, Poulidakos D. Pyramidal direct methanol fuel cells. *Int J Heat Mass Transf* 2006;49(7):1516–28.
- [36] Ramos-Alvarado B, Hernandez-Guerrero A, Elizalde-Blancas F, Ellis MW. Constructal flow distributor as a bipolar plate for proton exchange membrane fuel cells. *Int J Hydrogen Energy* 2011;36:12965–76.
- [37] Zhiwei F, Xinggui Z, Lingai L, Weikang Y. Experimental investigation of the flow distribution of a 2-dimensional constructal distributor. *Exp Therm Fluid Sci* 2008;33:77–83.
- [38] Tuber K, Oedegaard A, Hermann M, Hebling C. Investigation of fractal flow-fields in portable proton exchange membrane and direct methanol fuel cells. *J Power Sources* 2004;131:175–81.
- [39] Chen T, Liu S, Gong S, Wu C. Development of bipolar plates with different flow channel configurations based on plant vein for fuel cell. *Int J Energy Res* 2013;37:1680–8.
- [40] Murray CD. The physiological principle of minimum work: I. The vascular system and the cost of blood volume. *Proc Natl Acad Sci U. S. A* 1926;12(3): 207.
- [41] Thompson DW. On growth and form. Cambridge, UK: Cambridge University Press; 1942.
- [42] Bejan A, Lorente S. Design with constructal theory. Hoboken, N. J: John Wiley and Sons; 2008.
- [43] Liu Z, Zhang H, Wang C, Mao Z. Numerical simulation for rib and channel position effect on PEMFC performances. *Int J Hydrogen Energy* 2010;35(7): 2802–6.
- [44] Lee S, Jeong H, Ahn B, Lim T, Son Y. Parametric study of the channel design at the bipolar plate in PEMFC performances. *Int J Hydrogen Energy* 2008;33(20): 5691–6.
- [45] Nam JH, Kaviany M. Effective diffusivity and water-saturation distribution in single- and two-layer PEMFC diffusion medium. *Int J Heat Mass Transf* 2003;46(24):4595–611.
- [46] Van Nguyen T, White RE. A water and heat management model for Proton-Exchange-Membrane fuel cells. *J Electrochem Soc* 1993;140(8):2178–86.
- [47] Springer TE, Zawodzinski TA, Gottesfeld S. Polymer electrolyte fuel cell model. *J Electrochem Soc* 1991;138(8):2334–41.
- [48] Um S, Wang CY, Chen KS. Computational fluid dynamics modeling of proton exchange membrane fuel cells. *J Electrochem Soc* 2000;147(12):4485–93.
- [49] Jou D, Casas-Vazquez J, Lebon G. Extended irreversible thermodynamics. Heidelberg, Germany: Springer Berlin; 1996.
- [50] Bejan A. Entropy generation minimization: the method of thermodynamic optimization of finite-size systems and finite-time processes. Boca Raton, New York: CRC Press; 1995.
- [51] Damian-Ascencio CE, Hernandez-Guerrero A, Ascencio-Cendejas F, Juarez-Robles D. Entropy generation analysis for a PEM fuel-cell with a biomimetic flow field. In: Proceedings of the ASME 2009 international mechanical engineering congress and exposition, November 13–19, lake Buena Vista, Florida, USA; 2009.
- [52] Senn SM, Poulidakos D. Polymer electrolyte fuel cells with porous materials as fluid distributors and comparisons with traditional channeled systems. *J Heat Transf* 2004;126(3):410–8.
- [53] Um S, Wang CY. Three-dimensional analysis of transport and electrochemical reactions in polymer electrolyte fuel cells. *J Power Sources* 2004;125(1): 40–51.